View Article Online
View Journal

Energy & Environmental Science

This article can be cited before page numbers have been issued, to do this please use: J. Ren, P. Liu, Y. Qin, X. Yuan, X. Cao, T. Zhou and J. Zeng, *Energy Environ. Sci.*, 2026, DOI: 10.1039/D6EE01563H.

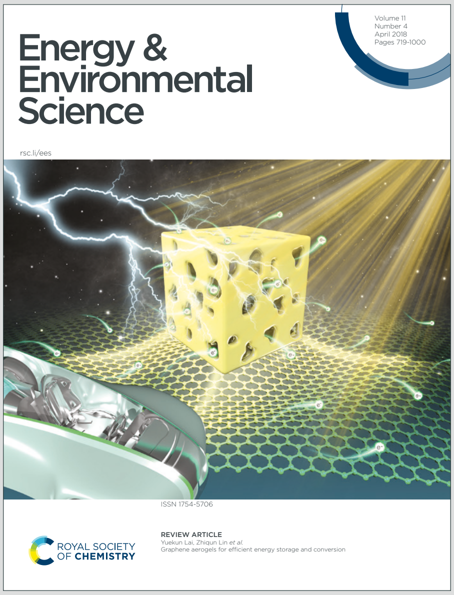

Volume 11
Number 4
April 2018
Pages 719-1000

Energy & Environmental Science

rsc.li/ees

ISSN 1754-5706

ROYAL SOCIETY OF CHEMISTRY

REVIEW ARTICLE
Yuekun Lai, Zhiqun Lin *et al.*
Graphene aerogels for efficient energy storage and conversion

ROYAL SOCIETY OF CHEMISTRY

rsc.li/ees

View Article Online
DOI: 10.1039/D6EE01563H

Direct air capture (DAC) is increasingly recognized as an essential climate mitigation solution by actively removing carbon dioxide excessively emitted. However, large-scale deployment remains constrained by the high energy demand of adsorbent regeneration, limited uptake capacity, and parasitic water evaporation. Many existing porous adsorbents (e.g., zeolites and MOFs) also lose performance in the presence of liquid water due to competitive adsorption. Here, we present a thermo-responsive DAC scheme based on lower critical solution temperature (LCST) phase transition, enabling a swell-adsorption/collapse-desorption mechanism that combines high CO_2 capture from air with low regeneration energy. The collaborative water-CO_2 adsorption/desorption along with the LCST swing transforms water from a challenge into privilege, thereby reducing thermal penalties. Enhanced CO_2 uptake at lower temperatures further supports applicability in cold areas. More broadly, this LCST-enabled concept offers insights into designing next-generation adsorbents to advance scalable carbon dioxide removal technologies and highlights route to coupling DAC with omnipresent low-grade waste heat sources.

View Article Online
DOI: 10.1039/D6EE01563H

Lower Critical Solution Temperature (LCST) Mediated Direct Air Capture of Carbon Dioxide with High Capacity and Low Regeneration Energy

Jiaxin Ren[1], Peigong Liu[1], Yuji Qin[1], Xi Yuan[1], Xiang Cao[1], Teng Zhou[1], Jian Zeng[1*]

[1]Sustainable Energy and Environment Thrust, Function Hub, The Hong Kong University of Science and Technology (Guangzhou), Nansha, Guangzhou, 511400, Guangdong, China

* Corresponding author:

E-mail addresses: jianzeng@hkust-gz.edu.cn.

Abstract

Direct air capture of carbon dioxide has been limited by the energy-intensive thermal regeneration of adsorbents imposed by the low CO_2 uptake capacity, high regeneration temperature and parasitic water evaporation. Herein, we demonstrated a class of thermo-responsive CO_2 adsorbents—PEI impregnated PNIPAM-grafted cellulose network (TRCNF/PEI)—achieving high CO_2 uptake of 2.82 mmol g^{-1} from air at 25 °C and 4.33 mmol g^{-1} at 5 °C, and low regeneration temperature below 65 °C. The thermo-responsive adsorbent features lower critical solution temperature (LCST) phase transition that enables a swell-adsorption/collapse-desorption mechanism. At room temperature, TRCNF/PEI is at a hydrophilic swollen state, effectively exposing the PEI amine sites for efficient CO_2 capture. Above LCST, it transitions to a hydrophobic collapsed state. Water is expelled in liquid phase, destabilizing bicarbonate intermediates and thereby driving rapid CO_2 desorption. This obviated the latent heat penalty of water, leading to unprecedentedly low regeneration thermal energy demand of 4.36 GJ ton^{-1}_{CO2} that can be satisfied solely by low-grade waste heat. Unlike zeolites activated carbons and MOFs vulnerable to high humidity where liquid water inhibits CO_2 uptake due to competitive adsorption, TRCNF/PEI leverages water to enhance adsorption and exhibits exceptional cyclic stability. Notably, the CO_2 uptake of TRCNF/PEI further increases at lower temperatures (4.33 mmol g^{-1} at 5 °C), demonstrating its carbon capture potential in cold area. The unique LCST phase transition presents a transformative strategy to couple DAC with vast low-grade industrial waste heat, significantly advancing the energy efficiency and durability of carbon removal technologies.

Keywords: Direct Air Capture; Thermo-responsive Adsorbent; Low-temperature Desorption; Lower Critical Solution Temperature (LCST); Carbon Dioxide

View Article Online
DOI: 10.1039/D6EE01563H

1.Introduction

An excess of thousands of giga metric tons of CO_2 (Gt_{CO2}) has been emitted into the atmosphere since industrialization.[1-2] With less than three decades to achieve carbon neutrality, in addition to rapid decarbonization, it is now also imperative to actively remove ~1 Gt CO_2 per year before 2030 to mitigate the global temperature overshoot.[3-5] Direct air capture (DAC) of carbon dioxide (CO_2), which selectively removes CO_2 from the atmosphere, is deemed as a pivotal negative emission technology to achieve this goal but it has been long impeded by the prohibitive land, energy, water and cost scaling limitations.[6-7] Conventional amine-grafted solid adsorbents (e.g., amine-grafted silicas or certain metal-organic frameworks) parallelly adsorb a significant amount of water (~18 $mmol_{water}$ g^{-1}) and require high temperature steam at 80–120 °C to overcome the heat of adsorption of CO_2 and water, sensible heat, and parasitic heat losses.[8] Furthermore, the co-adsorbed water in traditional amine-appended adsorbents often leads to severe amine leaching and oxidative degradation during high-temperature steam scrubbing, drastically limiting the adsorbent lifetime.[9-10] As a result, current DAC technologies consume 5–12 GJ of energy to capture 1 ton of CO_2 from air, 70% of which is in the form of heat,[11-13] translating into 10 Quads of energy to achieve the aforementioned milestone of removing 1 Gt CO_2 per year by 2050 (U.S. DOE, 2025).[14-16] This is equivalent to roughly 12% of global electricity consumption and is near-impossible, placing the 2050 target under serious threat.[17] To make matters worse, high regeneration temperature precludes the utilization of omnipresent low-grade waste heat sources (40–65 °C) such as from data centers,[18-19] power stations,[20] and so on.[21-22] Most DAC plants today are powered by grid electricity or natural gas,[23] leading to a high carbon intensity of ~0.73–1.1 kg_{CO2} emitted per unit kg of CO_2 captured due to the global average carbon footprint of grid (~486 g_{CO2} kWh^{-1}) and natural gas (~450 g_{CO2} kWh^{-1}).[17,24] To unlock the full potential of DAC, we must explore economically affordable and sustainable heat sources for thermal regeneration, such as low-grade waste heat from data centers and industrial processes at 40–65 °C, which remains inaccessible to most existing adsorbents.

Addressing these thermal and stability challenges necessitates a paradigm shift at the material level. Thermo-responsive polymers, notably poly(N-isopropylacrylamide) (PNIPAM), have attracted extensive attention due to their unique lower critical solution temperature (LCST) phase transition. Below the LCST (~32 °C), PNIPAM is in a hydrophilic state and exhibits affinity to water; upon heating above the LCST, it undergoes a sharp phase transition into a hydrophobic state and rapidly collapses. Water is released in the liquid phase without evaporative latent heat penalty. This reversible, temperature-driven steric reconfiguration has been widely explored to facilitate drug delivery,[25-27] smart surfaces,[28-32] and tissue engineering[33-35] and point source carbon capture.[36-37]

View Article Online
DOI: 10.1039/D6EE01563H

Recent studies revealed collaborative adsorption between CO_2 and water, i.e., water molecules promote CO_2 uptake kinetics and capacity due to enhanced proton transfer and formation of bicarbonate instead of ammonium carbamate compound.[8] It is thus possible to regulate the CO_2 uptake kinetics, capacity and desorption temperature by tuning the hydrophilicity of adsorbents, which warrants the development of thermo-responsive CO_2 adsorbents for DAC.

Herein, we report a class of thermo-responsive adsorbents for DAC that were synthesized from hyperbranched cellulose nanofibers (CNF) grafted with poly(N-isopropylacrylamide) (PNIPAM) and cross-linked with polyethyleneimine (PEI). This architecture leverages the unique LCST-mediated hydrophilic-hydrophobic transition to facilitate CO_2 uptake below LCST and rapid CO_2 desorption under mild heating. At ambient temperature (below LCST), the adsorbent is hydrophilic and swollen, exposing PEI sites to adsorb CO_2 and form carbonate groups, rendering a high CO_2 uptake of 2.81 mmol g^{-1} from air at 25 °C. Upon heating to 65 °C (above LCST), it transitions to hydrophobic state and release water in liquid phase, rapidly desorbing CO_2 by destabilizing the bicarbonate species without the latent heat penalty of water. By harnessing the LCST hydrophilic-hydrophobic transition, our adsorbents exhibited unprecedentedly high CO_2 uptake yet substantially lowered thermal energy demand of 4.36 GJ $ton^{-1}{}_{CO2}$, exclusively relying on low-grade waste heat below 65 °C. Crucially, unlike conventional amine-grafted solid adsorbents which are prone to amine leaching and oxidation at the presence of water, the crosslinked architecture of our adsorbent firmly anchors amine, guaranteeing both high water tolerance and exceptional durability over 500 cycles. This work therefore presents robust and energy-efficient adsorbent material that paves the way for scalable and energetically viable direct air capture.

2. Result and discussion

2.1. Synthesis and characterization of adsorbent

The design strategy for TRCNF/PEI is illustrated in Figure 1. First, thermo-responsive monomer NIPAM was grafted on the cellulose nanofibers (CNF) via Ce^{4+}-initiated radical polymerization.[38-39] The thermo-responsive PNIPAM-grafted cellulose nanofibers (TRCNF) was then in situ crosslinked with polyethyleneimine (PEI) via epichlorohydrin (ECH) into TRCNF/PEI adsorbents. More details of the synthesis of the TRCNF/PEI adsorbents can be found in Supporting information S1 section. Structural characterization via SEM and EDS reveals uniform morphology and elemental distribution (Figure S2). Below the LCST, the cellulose network remains in a swollen, hydrophilic state that favors CO_2 adsorption of amine sites due to enhanced proton transfer. When heated above the LCST, the NIPAM segment transitions to a hydrophobic state and undergoes a coil-to-globule contraction. Water molecules are repelled from the cellulose network in liquid phase (Figure S3 and Supplementary Video 1), which facilitates CO_2 desorption by destabilizing the

View Article Online
DOI: 10.1039/D6EE01563H

bicarbonate group. Released liquid water could be easily separated and collected before evaporation under continuous hot gas flow (Figure S4a and Supplementary Video 2), with no detectable leaching of amine or polymer from the adsorbent (Figure S4b and Figure S4c). Therefore, latent heat penalty of water could be avoided. This temperature-induced hydrophilic-hydrophobic switch of TRCNF/PEI is evidenced by different water sorption performance at below LCST (142% at 25 °C, 95% RH) and above LCST (0.05% at 65 °C, 95% RH) (Figure S5). The TRCNF and PEI mass ratio was engineered to maximize the CO_2 capture efficiency and exhibited the optimal performance at a TRCNF: PEI mass ratio of 1:22 (calculated based on their exact dry solid masses, equivalent to the molar ratio of 1:3.76) (Figure S6). Lower PEI loading leads to deficit of active amine sites for chemisorption while excessive PEI loading forms dense crosslinked network that impedes CO_2 diffusion, as evidenced by its lower equilibrium swelling ratio (480% compared to 600% for TRCNF/PEI (1:22), as shown in Figure S7a).[40-41] The N_2 adsorption/desorption isotherms analysis shows that the BET specific surface areas of TRCNF/PEI (1:22) is larger than that of TRCNF/PEI (1:24) (Figure S7b). Therefore, the TRCNF: PEI mass ratio of 1:22 was chosen for all subsequent experiments.

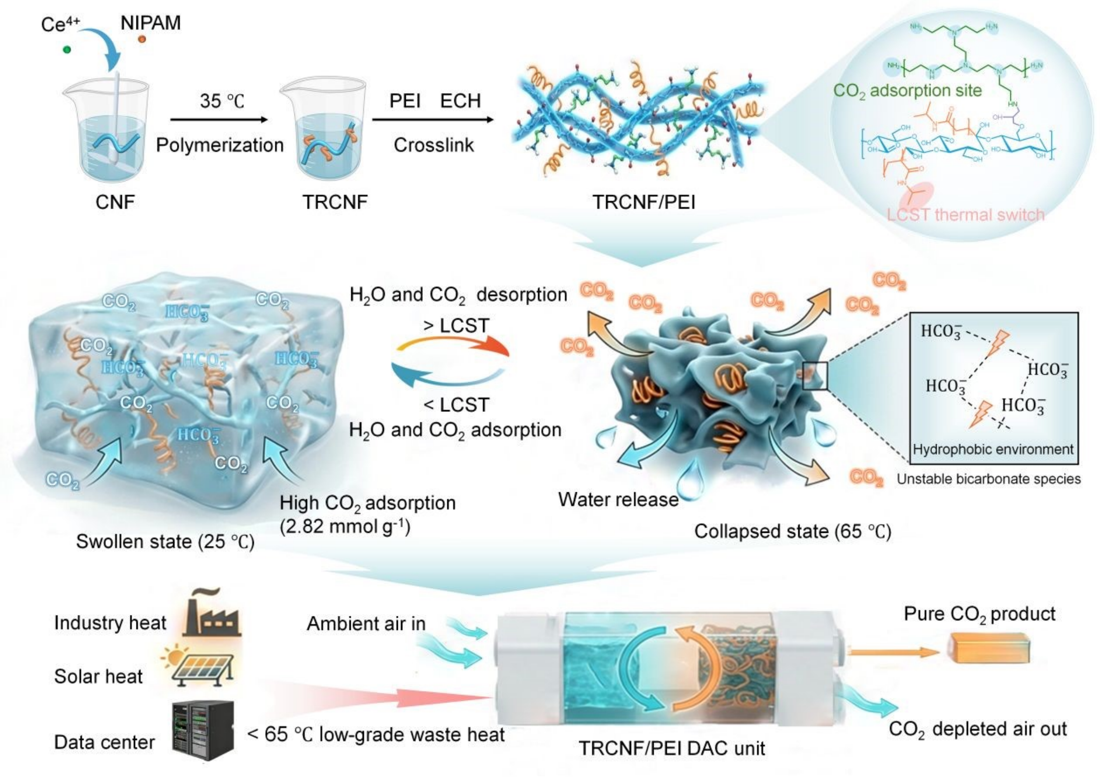

Figure 1. Synthesis and working principle of the thermo-responsive TRCNF/PEI adsorbent for energy-efficient direct air capture (DAC) of CO_2. The hyperbranched cellulose nanofibers (CNF) are grafted with temperature-responsive PNIPAM and crosslinked with PEI to form a robust three-dimensional network. Below the LCST (at 25 °C), the hydrophilic/swollen state facilitates CO_2 uptake; above the LCST (at 65 °C), the hydrophobic/collapsed state triggers rapid CO_2 desorption

View Article Online
DOI: 10.1039/D6EE01563H

and liquid water expulsion in liquid phase. The low regeneration temperature and evaporation-free desorption warrant integration of DAC with low-grade waste heat to minimize thermal energy consumption.

The structure and chemical composition of the adsorbent were rigorously characterized by a series of spectroscopies. The solid-state ^{13}C nuclear magnetic resonance (NMR) spectroscopy of pristine CNF revealed the typical carbon signals of Cellulose I (C1–C6), with a distinct peak at δ = 179 ppm (Peak 7) corresponding to the carbonyl carbon of the carboxyl groups (–COOH) (Figure 2a).[42] After successful grafting with temperature-responsive PNIPAM and crosslinking with PEI, a new near-baseline hump peak at 165 ppm occurred, corresponding to the carbonyl carbons (C=O) of amide and carboxyl groups (Figure 2b). A series of intense peaks emerged in the high-field region (20–60 ppm), corresponding to the methylene carbons ($-CH_2-CH_2-NH-$) of the PEI backbone and the aliphatic carbons (isopropyl and main chain methylene) of the PNIPAM side chains. The successful grafting of PNIPAM was also validated by the ^{1}H NMR analysis (Figure S8), which identified characteristic peaks at δ = 0.8 ppm (methyl protons of isopropyl) and δ = 4.2 ppm (methine proton of isopropyl). The ^{1}H NMR signals at δ = 3.2 ppm (methylene protons) validated the presence of PEI chains.

The successful integration of organic amines and thermo-sensitive polymers onto the cellulose nanofibers was cross-validated by Fourier transform infrared spectroscopy (FT-IR, Vertex 70V + Hyperion II) (Figure 2c). Pristine CNF exhibits a broad O–H stretching band at ~3300 cm^{-1} and characteristic COO^- IR peaks at 1600-1700 cm^{-1}.[43] With PNIPAM grafted (TRCNF), the fingerprint peaks appear at 1655 cm^{-1} (Amide I band, C=O stretching) and 1544 cm^{-1} (Amide II band, N–H bending) corresponding to the amide groups in PNIPAM (Figure S9). Furthermore, the distinct doublet at 1387 cm^{-1} and 1368 cm^{-1} corresponds to the symmetric bending vibrations of the methyl groups in the *N*-isopropyl segment. Following the loading of PEI (TRCNF/PEI), prominent adsorption peaks emerged at 2930 and 2800 cm^{-1}, which are assigned to the C–H stretching vibrations of the methylene ($-CH_2-$) units in the PEI backbone. The intensity of these peaks is significantly higher compared to TRCNF, verifying the incorporation of PEI chains within the 3D intertwined network. Additionally, the broad band centered at ~3300 cm^{-1} widens, attributed to the overlapping of N–H stretching vibrations from PEI amines with the O–H bands of cellulose, suggesting the formation of a dense hydrogen-bonding network. Meanwhile, the strong characteristic peak of the cellulose skeleton (C–O–C stretching) at 1030–1060 cm^{-1} was well-preserved, indicating that the multi-step modification did not compromise the structural integrity of the CNF framework.

The active amine sites for CO_2 chemisorption were quantified by X-ray photoelectron spectroscopy (XPS, ULVAC-PHI VersaProbe4). The PEI grafting was noted by the distinct N 1s emission peak at ~400 eV, which was absent in the pristine CNF (Figure 2d).[44] Quantitative analysis

View Article Online
DOI: 10.1039/D6EE01563H

indicates that the TRCNF/PEI surface is predominantly composed of C (61.6 at%), N (22.5 at%), and O (15.9 at%) (Figure S10). The high nitrogen content confirms active amine site in TRCNF/PEI. The high-resolution N 1s spectrum (Figure 2e) was deconvoluted into four distinct peaks, i.e., amide groups (399.99 eV, 13.8%), tertiary amines (3°, 398.90 eV, 23.0%), primary amines (1°, 398.38 eV, 51.1%), and secondary amines (2°, 397.90 eV, 12.1%). The active amine sites, i.e., 1°, 2°, and 3° together as the primary chemisorption sites for CO_2, account for 86.2% of the total nitrogen species. Based on these quantitative XPS data, the theoretical total amine density is estimated to be 14.82 mmol g^{-1}, and is dominated by primary amines (8.78 mmol g^{-1}), suggesting the potential of TRCNF/PEI for high-capacity CO_2 capture. We also analyzed the C 1s and O 1s spectra to corroborate the successful grafting of PNIPAM and the subsequent integration of the PEI network onto the cellulose matrix (Figure S11).

The thermal stability of TRCNF/PEI was evaluated by thermogravimetric analysis (TGA, TA 5500) (Figure 2f). The curve remains stable in the range of 100–280 °C, proving that the adsorbent was thermal stably at the typical regeneration temperature < 65 °C. A sharp mass loss occurred at 280 °C due to the pyrolysis of the PEI and PNIPAM organic chains. The mass loss above 280 °C was found substantially higher in TRCNF/PEI than in pristine CNF, which confirms the high loading of PEI and PNIPAM in the adsorbent.

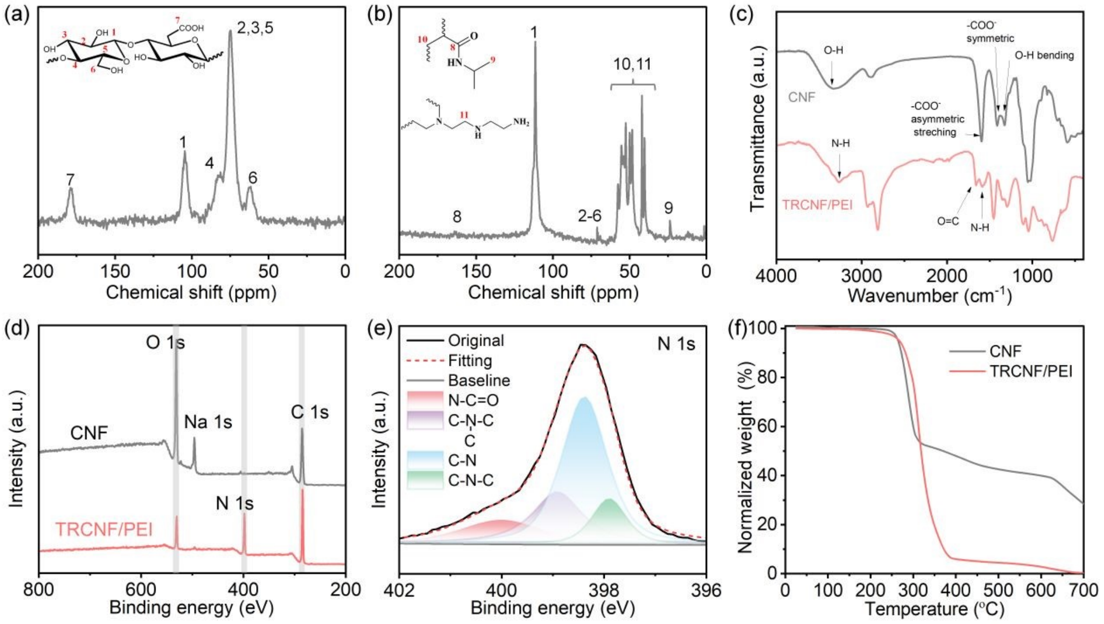

Figure 2. Spectroscopic analysis and thermal stability of TRCNF/PEI. ^{13}C solid-sate NMR spectra of (a) pristine CNF and (b) TRCNF/PEI, highlighting the characteristic signals of cellulose backbone, grafted PNIPAM and crosslinked PEI. c) FT-IR spectra of CNF and TRCNF/PEI. d) Full scan XPS spectra of CNF and TRCNF/PEI. e) High-resolution N 1s XPS spectra for TRCNF/PEI, along with peak deconvolution to quantify the chemical states of different amine groups. f) Thermogravimetric analysis of CNF and TRCNF/PEI samples under nitrogen atmosphere. The

View Article Online
DOI: 10.1039/D6EE01563H

samples were first heated at 90 °C for 60 min to ensure complete removal of adsorbed moisture prior to thermal stability assessment.

2.2. Performance of LCST-mediated CO_2 adsorption-desorption

The CO_2 adsorption and desorption performance in 400 ppm CO_2 stabilized in 1 bar N_2 of the TRCNF/PEI adsorbents was evaluated by fixed-bed breakthrough experiments. Details of the experimental procedures can be found in Supporting Information. In brief, 0.5 g of dry adsorbent was hydrated to achieve 600 wt% water content and then was loaded into an adsorption column of 1 cm in diameter with the simulated gas stream flowing through it at 25 °C. The CO_2 adsorption performance was obtained by monitoring the outlet CO_2 concentration using an online mass spectrometry (MS, INFICON) and the cumulative CO_2 uptake was calculated by the area between the inlet concentration baseline and the outlet breakthrough curve.

The CO_2 uptake was found sensitive to the initial hydration state of the adsorbent (Figure 3a). The dry adsorbent (0% water content) barely adsorbed CO_2 despite fast saturation at the breakthrough time of 0.05 h (Figure 3b). In distinct contrast, the pre-hydrated adsorbent (initial water content of 600 wt%) exhibited an excellent adsorption capacity of 2.82 mmol g^{-1}. It showed a typical S-shaped adsorption curve, reaching 1.41 mmol g^{-1} (50% saturation) at 14.2 h and 2.26 mmol g^{-1} (80% saturation) at 23.1 h. The S-shaped breakthrough profile indicates potential diffusional resistances in overall CO_2 uptake kinetics. This distinct difference highlights a key feature of our material: unlike conventional amine-grafted solid adsorbents (e.g., amine-grafted metal-organic frameworks such as Mg_2(dobpdc)(3-4-3)) or certain zeolite-based materials) where water can hinder CO_2 capture, the presence of water facilitates CO_2 uptake in TRCNF/PEI. The presence of pre-loaded water promotes both CO_2 diffusion via adsorbent swelling and CO_2 chemisorption by favoring the formation of bicarbonate intermediates. It has been long acknowledged that under dry conditions, CO_2 binds with primary/secondary amines through a bimolecular mechanism to form carbamates ($R\text{-}NHCOO^-$), which requires two amine groups to fix one CO_2, whereas with the presence of water molecules, which act as efficient proton-transfer mediators, the formation of bicarbonate intermediates ($R\text{-}NH_3^+$ and HCO_3^-) is kinetically and thermodynamically favored, enabling one amine group to independently capture one CO_2. This not only improves amine utilization efficiency but also activates otherwise inert tertiary amine sites. Prior studies have also found the enhanced CO_2 uptake kinetics due to enhanced proton transfer by water molecules.[8] In addition, thanks to the hydrophilic nature of TRCNF/PEI below LCST, the adsorbent remains hydrated and swollen in humid environments, expanding the originally dense cellulose-based network into an open structure. CO_2 diffusion is facilitated in enlarged internal pores and the sterically hindered amine groups are exposed to CO_2 molecules. Multiple identical samples were prepared to be pre-hydrated at different levels for parametric study. The water-facilitated CO_2

View Article Online
DOI: 10.1039/D6EE01563H

adsorption can be further validated by the progressive CO_2 uptake from 0.05 mmol g^{-1} in dry state (0% water content) to 2.62 mmol g^{-1} at 500% water content (Figure S12). CO_2 concentration-dependent adsorption found that CO_2 adsorption in TRCNF/PEI was reaction dominated, validated by the high CO_2 uptake ~6.5 mmol g^{-1} with reduced breakthrough (< 3 min) in 10% CO_2 stabilized in 1 bar N_2 (Figure S13).

The critical advantage of TRCNF/PEI over conventional amine-grafted solid adsorbents lies in its low regeneration temperature and water evaporation-free CO_2 desorption. As illustrated in Figure 3c, the adsorbents completely desorbs CO_2 under mild heating at 65 °C (above LCST, by purging 65 °C dry 1 bar N_2 stream) opposed to 80–120 °C hot steam routinely used in PEI-grafted adsorbents .[10, 19] The amount of desorbed CO_2 was calculated by integrating the downstream CO_2 concentration over time. At 65 °C, 5 hours was needed to desorb all the adsorbed CO_2. The adsorbent underwent 15 adsorption-desorption cycles by LCST temperature swing (Figure 3d) and maintained a consistently high CO_2 uptake of 2.82 mmol g^{-1} for all cycles. This exceptional cyclic stability highlights the inherent robustness of our crosslinked architecture, featuring covalent immobilization of amine functionalities that effectively prevent PEI leaching even in the presence of water. This unique feature allows the material to harness water for enhanced CO_2 capture without compromising the long-term performance. Overall, the consistent adsorption-desorption performance under both simulated air (400 ppm CO_2) and concentrated CO_2 conditions underscores the functionality and durability of TRCNF/PEI, establishing a strong basis for practical direct-air-capture applications.

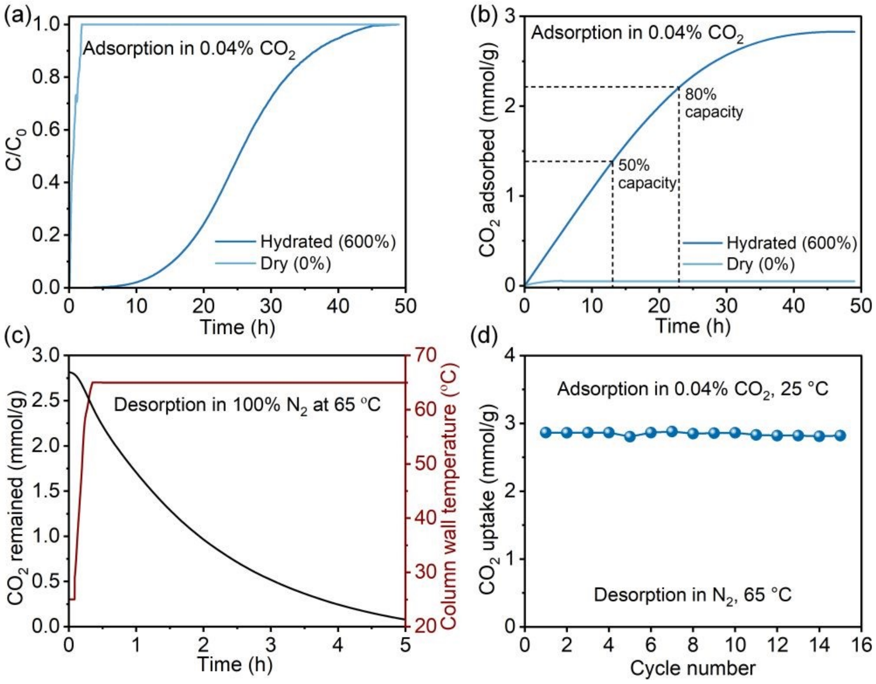

Figure 3. DAC performance of TRCNF/PEI adsorbents. a) CO_2 breakthrough curves of TRCNF/PEI with different water contents (600 wt% and 0%) under simulated air (400 ppm CO_2 in N_2) at 25 °C. b) The corresponding cumulative CO_2 adsorption capacity derived from (a). c) CO_2

View Article Online
DOI: 10.1039/D6EE01563H

desorption profile of the saturated sample under 1 bar pure N_2 flow at 65 °C. d) Cyclic stability test showing CO_2 uptake over 15 adsorption (25 °C)-desorption (65 °C) cycles. Prior to each adsorption cycle, the adsorbent was rehydrated to its initial water content (600 wt%) to ensure a consistent starting state.

2.3. Mechanistic origin of LCST-mediated regeneration

To unravel the molecular mechanism of LCST phase transition-induced desorption, *in situ* diffuse reflectance infrared Fourier transform spectroscopy (DRIFTS, Thermo IS 50) and dynamic light scattering (DLS, Malvern Zetasizer Ultra) analyses were performed (See Experimental Section for details). For DRIFTS measurements, the dry adsorbent was placed in 400 ppm humid CO_2 (~100% relative humidity, achieved by bubbling CO_2 through water) in 1 bar N_2 at 25 °C and the evolving FTIR spectra were recorded during CO_2 adsorption. After saturation, the adsorbent was progressively heated up under dry N_2 flow for CO_2 desorption and the FTIR spectra were recorded at each temperature after equilibrium. In parallel, DLS measurements were performed on pre-hydrated TRCNF/PEI samples (600 wt% water content) to track the particle size evolution during temperature-induced phase transition. During CO_2 adsorption at 25 °C, the signature peaks of CO_2 adsorption at 1715 cm^{-1} (C=O stretching of bicarbonate) and water adsorption 3640 cm^{-1} (O–H stretching of adsorbed water) were found to synchronously intensified over time (Figure 4a, b).[45-49] The synergy between the two peaks manifests the formation of water-stabilized bicarbonate species. To provide robust evidence of the chemisorption nature of CO_2 uptake, we performed ^{13}C solid-state NMR spectroscopy on our adsorbent. The new peaks at 165.2 ppm after CO_2 adsorption manifests the formation of water-stabilized bicarbonate species (Figure S14). During desorption under dry N_2 purge (Figure 4c, d), both peaks decayed concurrently and vanished eventually as temperature increased from 25 °C to 65 °C. To better elucidate the collaboration between LCST transition and CO_2 desorption, we correlated the temperature, normalized IR peak intensities and average particle diameter measured by DLS (red line in Figure 4d). The intensity of all IR peaks was normalized to that at 25 °C. Upon heating above the LCST (32 °C), the particle size of TRCNF/PEI gradually shrunk from ~6 μm to ~1 μm as temperature increased from 32 °C to 55 °C, indicating that the adsorbent transitioned to the hydrophobic collapsed state. As the cellulose-based network collapsed, water was fully expelled from the adsorbent indicated by the vanishing O–H stretching peak of adsorbed water (3640 cm^{-1}). The loss of water then triggers the destabilization of bicarbonate species, leading to rapid CO_2 desorption, evidenced by the vanish of C=O stretching peak of bicarbonate following the O–H stretching of adsorbed water. The schematic in the lower panel of Figure 4d illustrates this cascade: the hydrophobic collapse of cellulose network expels the solvated water, which in turn destabilizes the bicarbonate intermediates, ultimately forcing CO_2 desorption. This

View Article Online
DOI: 10.1039/D6EE01563H

physical mechanism explains the negligible CO_2 affinity (0.05 mmol g^{-1}) at 65 °C and rationalizes the high regeneration efficiency achieved under mild heating (Figure S15).

The LCST-induced adsorbent collapse was also validated by molecular dynamics (MD) simulations (See Supporting Information Section S11 for details). In brief, we tracked the dynamic trajectories of the hydrophilic domains (comprising the CNF and PEI backbones) and the hydrophobic isopropyl segments of the PNIPAM side chains at 25 °C and 65 °C. We used the radius of gyration (R_g) and solvent accessible surface area (SASA) to quantify conformational evolution (Figure 4e and Figure 4f). At 25 °C (below LCST), the PNIPAM segments of TRCNF/PEI formed stable hydrogen bonds with water molecules. Consequently, the chain maintained an extended, well-solvated conformation, characterized by a stable R_g (~23 Å) and a relatively high SASA throughout the simulation. Snapshots in the Supporting Information (Figure S16) confirm that the cellulose-based network remains expanded with no significant aggregation at 25 °C. In contrast, at 65 °C (above LCST), intensified thermal vibrations first broke the hydrogen bonds between water molecules and the PNIPAM amide groups, a process marked by a temporary kinetic expansion and an R_g spike within the initial 20 ns (Figure 4e). Freed from these stabilizing hydrophilic interactions, the chain's behavior was then dominated by hydrophobic forces among the isopropyl segments. This shift triggered an LCST-driven collapse—a thermodynamically favorable aggregation of adsorbent that expelled bound water—ultimately resulting in a stable, compact state characterized by a lower R_g and a ~14% reduction in SASA to ~12,000 $Å^2$ (Figure 4f). This thermally induced collapse is visually corroborated by the snapshots in Figure 4g, where the cellulose-based network transitions from a loose coil (0 ns) to a compact globule structure (50 ns). These simulation results show similar trends to the DLS and in situ DRIFTS tests, together with macroscopic optical observations supporting the thermally induced hydrophobic coil-to-globule collapse (Figure S17 and video 3). While this significant volume shrinkage, crucial for adsorbent regeneration, could cause voids and airflow channeling in packed beds, it is not an insurmountable engineering challenge. Practical DAC reactor designs can effectively ensure macroscopic bed volume stability, and thus fully leverage the material's advantages, by integrating the active hydrogel into structured contactors such as coatings on honeycomb monoliths, open-cell foams, or hollow fiber surfaces. This approach ensures stable operation and efficient regeneration in practical DAC applications.[50-52]

View Article Online
DOI: 10.1039/D6EE01563H

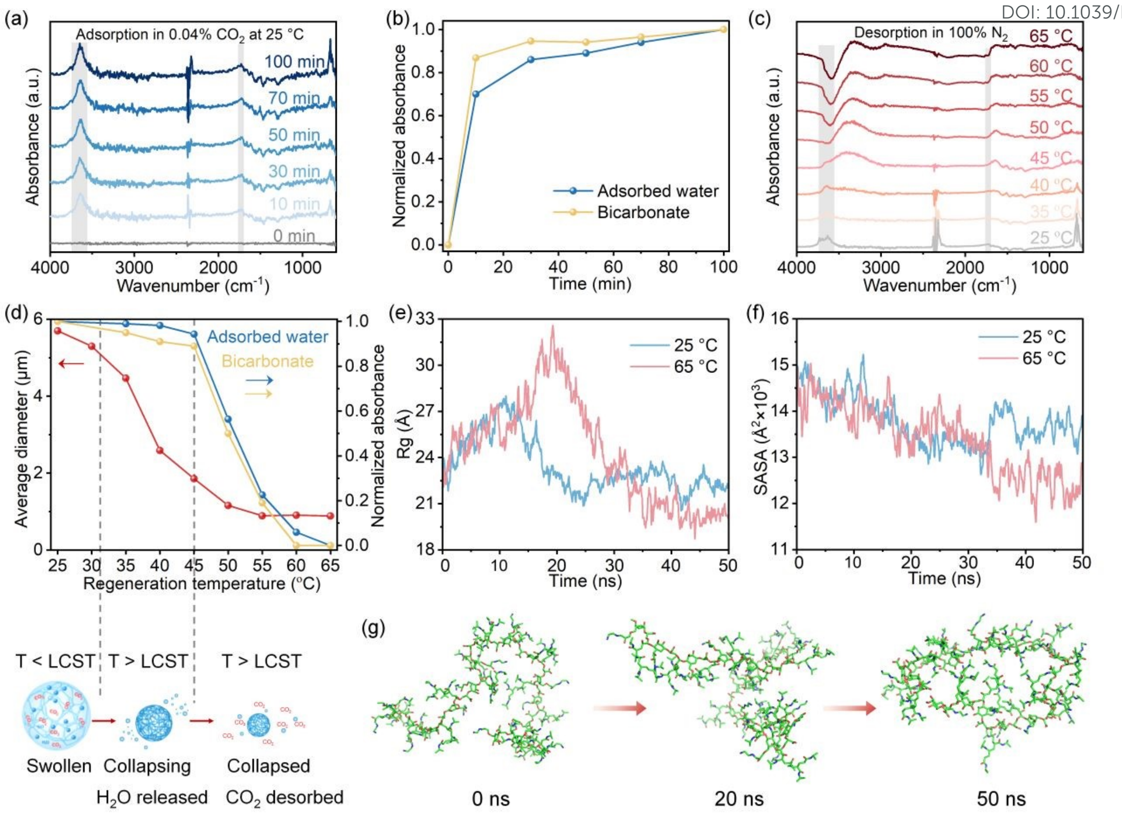

Figure 4. Molecular mechanism of LCST-triggered CO_2 desorption. a) Time-dependent *in-situ* DRIFTS spectra during CO_2 adsorption at 25 °C and (b) the corresponding normalized intensity evolution of peaks at 3640 cm^{-1} (adsorbed water) and 1715 cm^{-1} (bicarbonate) to that at t = 0. c) Temperature-dependent *in-situ* DRIFTS spectra during desorption and (d) Correlation between temperature-dependent structural collapse and CO_2 desorption: average particle diameter measured by DLS (red line) and normalized IR peak intensities of adsorbed water (blue line) and bicarbonate (yellow line) as a function of regeneration temperature, with schematic illustration of the LCST-induced desorption mechanism (lower row). e) Radius of gyration (R_g) and (f) Solvent-accessible surface area (SASA) of TRCNF/PEI over a 0–50 ns period at 25 °C and 65 °C. g) Representative MD simulation snapshots of the TRCNF/PEI molecular chain at 65 °C, visualizing the conformational transition from a solvated coil (0 ns) to a collapsed globule (50 ns).

2.4. Levelized energy analysis and cyclic stability

The feasibility of TRCNF/PEI for practical DAC deployment is highlighted by its exceptional energy efficiency and durability. Our material achieves exceptional CO_2 uptake capacity for DAC (~2.82 mmol g^{-1}) at a significantly reduced regeneration temperature (65 °C) compared to the state-of-the-art (Figure 5a, detailed data see Supplementary Table 1). To quantify energetic advantage of TRCNF/PEI, we decoupled the regeneration energy components using simultaneous TGA-DSC analysis equipped with a DSC sensor (Figure S18). The total regeneration energy (Q_{total}) was deconvoluted into three components (Figure 5b): the sensible heat required to heat the sorbent itself (Q_{sens}), the enthalpy of CO_2 desorption (ΔH_{CO2}), and the heat associated with water released by LCST effect (Q_{H2O}).[53-55] Q_{H2O} generally constitutes a major energy budget of 3–10 GJ ton_{CO2}^{-1} to conventional DAC using MOFs/COFs due to the latent heat penalty for water evaporation.[8] However, different from water desorption in vapor phase in conventional amine-grafted solid adsorbent (e.g., amine-grafted metal-organic frameworks), our adsorbents release water in the liquid phase in LCST transition and avoids the latent heat penalty (Figure S19). Consequently, the energy required for water expulsion is reduced to 1.54 GJ ton^{-1}_{CO2}. It is important to note that energy estimations, including those in Table S2, generally exclude auxiliary components such as fans. In addition, the levelized sensible heat and heat of CO_2 desorption are also reduced due to the high CO_2 uptake. The levelized energy of CO_2 capture for TRCNF/PEI reaches an unprecedently low level of 4.36 GJ ton^{-1}_{CO2}, which is 25–65% lower than commercial liquid MEA (10.7 GJ ton^{-1}_{CO2})[54] or solid adsorbents like Mg_2(dobpdc)(3-4-3) (11.4 GJ ton^{-1}_{CO2}),[8] and COF-999 (5.9 GJ ton^{-1}_{CO2}).[57] The levelized energy of TRCNF/PEI is close to the enthalpy of amine (2 GJ ton^{-1}_{CO2}) and is only 3.9 GJ ton^{-1}_{CO2} higher than the thermodynamic limit of separating 400 ppm CO_2 from air (i.e., reaching 10.6% second-law efficiency). More importantly, the thermal energy for TRCNF/PEI can be sufficiently satisfied by omnipresent low-grade heat < 65 °C while contemporary DAC pilot plants rely on high-grade energy like electricity and natural gas.

The materials were stress-tested at the desorption temperature of 80 ℃, which was much higher than the operational temperature. Therefore, the predicted lifetime represents a conservative estimation. The TRCNF/PEI was stress-tested under accelerated swing between 25 °C, 0.04% CO_2, ~100% RH for 5 h for adsorption and 80 °C, 100% N_2, 0% RH for 2 h for desorption (Figure 5c inset and Figure S22). After 500 cycles, the TRCNF/PEI material retains high capacity with negligible degradation (Figure 5c). The working capacity stabilized at ~1.93 mmol g^{-1}, retaining 96.5% of its initial cycling capacity (2.00 mmol g^{-1}). Surface chemical stability was confirmed by the minimal change (≤ 1.2%) in atomic percentages of O, N, and C (Figure S23). Beyond dry regeneration, the material's adaptability to realistic DAC conditions was also thoroughly investigated using TGA, including the presence of humidity and varying regeneration temperatures. Desorption kinetics under humid N_2 carrying gas flow (~100% RH) at 80 °C revealed 100% complete regeneration within 70 minutes (Figure S24). Furthermore, complete CO_2 desorption could be achieved in approximately 30 minutes at 65 °C, and significantly faster at higher temperatures, requiring only about 10 minutes at 85 °C (Figure S25a). While a pure CO_2 atmosphere slightly extended the full regeneration time to ~50 minutes (Figure S25b, compared to ~19 minutes in N_2), this remains practically manageable, especially with the application of vacuum or elevated temperatures. This versatility means that the regeneration temperature can be adjusted from 60–85 °C to efficiently match available low-grade waste heat, guaranteeing both complete CO_2 removal

View Article Online
DOI: 10.1039/D6EE01563H

and >95% purity. Additional cyclic TGA tests at 75 and 85 °C (Figure S26) confirmed excellent stability at elevated temperatures over 10 cycles, showing minimal changes in CO_2 uptake kinetics and capacity. Finally, long-term cycling under humid simulated air (0.04% CO_2, 21% O_2 in N_2, ~100% RH) demonstrated remarkable oxidative stability, with the adsorbent preserving 90.6% of its original CO_2 uptake and minimal amine loss after 53 cycles (Figure S27), further confirming the robustness of TRCNF/PEI for practical DAC operation. This stability highlights a critical advantage over conventional amine-appended solid adsorbents, where moisture often induces severe amine leaching and degradation. The elongated lifetime of our adsorbent is attributed to the much milder regeneration condition than status-quo using high temperature steam for aggressive CO_2 extraction. Notably, the TRCNF/PEI exhibits promising DAC performance at sub-ambient temperatures, achieving a CO_2 uptake of 4.33 mmol g^{-1} at 5 °C (Figure S28), and its synthesis is readily scalable using commercially available precursors (~10 USD kg^{-1} laboratory grade, significantly lower at scale), coupled with its straightforward synthesis process, positioning TRCNF/PEI as a highly promising, robust, and economically practical candidate for large-scale DAC deployment.

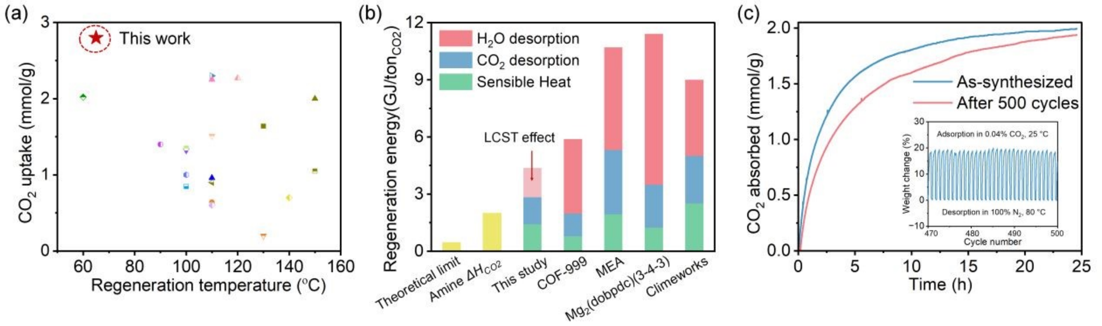

Figure 5. Levelized energy analysis and cyclic stability of TRCNF/PEI. a) Performance comparison with state-of-the-art amine-based adsorbents regarding CO_2 capacity and regeneration temperature. b) Deconvolution of levelized energy consumption into three components: sensible heat (green), CO_2 desorption (blue), and water desorption (red). The regeneration energy of TRCNF/PEI is compared with theoretical limits, hydrophilic liquid MEA, hydrophilic Mg_2(dobpdc)(3-4-3), hydrophobic COF-999 and Climeworks company. References provided in Table S2. c) TGA-derived adsorption curves for TRCNF/PEI before (blue) and after 500 cycles (red). Each of the 500 intermediate cycles employed a 5-hour adsorption and 2-hour desorption step to accelerate cyclic aging, while the 0st cycle first and 501st cycles (shown) used a 25-hour adsorption step to reach equilibrium and enable accurate capacity comparison. Inset**:** Detailed weight change profiles during cycles 470–500 under simulated DAC conditions (Adsorption: 25 °C, 0.04% CO_2, ~100% RH; Desorption: 80 °C, 100% N_2, 0% RH).

View Article Online
DOI: 10.1039/D6EE01563H

3. Conclusion

In summary, we have developed a class of thermo-responsive CO_2 adsorbent for DAC with unique LCST-mediate hydrophilic-hydrophobic transition to address the critical energy and stability bottlenecks in DAC. The TRCNF/PEI adsorbent exhibits exceptional CO_2 capture capability (2.82 mmol g^{-1} at 25 °C, which increases to 4.33 mmol g^{-1} at 5 °C) and rapid regeneration at a mild temperature of 65 °C. The enhanced performance at lower temperatures, driven by stronger hydration and increased amine accessibility, underscores the material's potential for DAC operation in cold area. Multidimensional spectroscopic analyses (*in-situ* DRIFTS and DLS) reveal that the regeneration mechanism is driven by the thermally induced hydrophobic collapse of the PNIPAM network. This structural contraction expels water molecules essential for stabilizing bicarbonate species, effectively shifting the chemical equilibrium towards CO_2 release. It obviates the sensible heat penalty for high-temperature regeneration, latent heat penalty of water evaporation, and aggressively out-of-equilibrium temperature-pressure swing in conventional amine-grafted solid adsorbents, leading to unprecedently low levelized energy of 4.36 GJ $ton^{-1}{}_{CO2}$ and exceptional material durability. The crosslinked architecture of our adsorbent anchors amine and avoid leaching in the presence of water, which has been a challenge to conventional amine-appended solid adsorbents, leading to long-term stability over 500 cycles. This work provides a generic paradigm for designing energy-efficient and scalable adsorbent materials to overcome the long-existing adsorbent performance barrier impeding rapid scale-up of DAC.

4. Experimental Section

Details of the synthesis, characterization, and molecular dynamics simulation are explained in the Supporting Information.

4.1 Cyclic adsorption-desorption stability test using dynamic breakthrough measurements

The cyclic adsorption-desorption performance was evaluated on the BSD-MAB breakthrough analyzer equipped with a mass spectrometer (MS, INFICON) for real-time monitoring of CO_2 concentrations. Dry TRCNF/PEI (0.5 g) was hydrated to achieve a water content of 600 wt% and then was packed into a glass column (inner diameter = 1 cm). Each cycle comprised: (1) Adsorption at 25 °C under humidified 400 ppm CO_2/N_2 flow (50 mL min^{-1}) until breakthrough equilibrium; (2) Desorption at 65 °C under dry N_2 flow (50 mL min^{-1}) until complete CO_2 release. The temperature was controlled by the column wall heater, and the system was cooled to 25 °C between cycles. Before each subsequent breakthrough cycle, water was manually replenished to restore the adsorbent to its target hydrated state (600 wt% water content). A total of 15 consecutive cycles were performed. The amount of adsorbed CO_2 was determined by integrating the area between the inlet concentration baseline and the outlet breakthrough curve; (3). The cyclic stability was assessed by comparing the CO_2 uptake capacity across all cycles.

4.2 Accelerated aging of adsorbents using Thermogravimetric

The cyclic adsorption and desorption behavior of TRCNF/PEI was evaluated using a Mettler Toledo TGA/DSC 3+ analyzer. A customized gas mixing system was employed to generate humidified streams by bubbling dry gases through a water saturator. Before the cycling test, approximately 5 mg of the sample was activated at 100 °C under a dry N_2 flow (50 mL min^{-1}) for 20 min to remove pre-adsorbed moisture and impurities, followed by cooling to 25 °C. The long-term stability test consisted of 500 consecutive adsorption-desorption cycles. Each cycle comprised two steps: (1) Adsorption: The sample was exposed to a humidified CO_2 stream (400 ppm CO_2 in N_2, ~100% RH) at 25 °C for 5 h; (2) Desorption: The temperature was ramped to 80 °C under a dry N_2 flow (50 mL min^{-1}) and maintained for 2 h to ensure complete regeneration. The humid adsorption gas was generated by passing the feed gas through a water bubbler, such that the adsorbent was rehydrated in situ during each adsorption step and no manual water addition was required between cycles. The 0st cycle first and 501st cycles (shown) used a 25-hour adsorption step to reach equilibrium and enable accurate capacity comparison. The working capacity for each cycle was calculated based on the mass change between the adsorption and desorption endpoints. The elevated regeneration temperature of 80 °C was deliberately selected as an accelerated aging condition to stress-test the adsorbent under significantly higher-than-normal temperature. The lifetime estimated here thus represents a conservative scenario. To further evaluate oxidative stability, an additional TGA cycling test was performed under humidified simulated air containing 21% O_2. In this experiment, each cycle consisted of adsorption at 25 °C for 5 h under 0.04% CO_2, 21% O_2 in N_2 at ~100% RH by flowing feed gas through a water bubbler, followed by desorption at 80 °C for 2 h under dry N_2 (50 mL min^{-1}). A total of 53 consecutive cycles were conducted.

4.3 *In situ* DRIFTS measurements

In situ diffuse reflectance infrared Fourier transform spectroscopy (DRIFTS) measurements were performed using a Thermo IS50 spectrometer equipped with an *in-situ* reaction cell over a wavenumber range of 400–4000 cm^{-1}. Prior to the adsorption, the sample was pretreated in a N_2 flow of 50 mL min^{-1} at 100 °C for 30 min (heating rate: 10 °C min^{-1}) to remove adsorbed impurities. After the sample cooled naturally to 25 °C and stabilized for 15 min, a background spectrum was collected. Adsorption was initiated by switching the feed gas to a humidified CO_2 stream (400 ppm CO_2 balanced in N_2, flow rate: 50 mL min^{-1}). Subsequently, the regeneration mechanism was investigated by switching the atmosphere back to dry N_2 (50 mL min^{-1}). A stepwise temperature-programmed desorption method was employed, where the sample was heated from 25 °C to 65 °C

View Article Online
DOI: 10.1039/D6EE01563H

in 5 °C increments (heating rate: 10 °C min^{-1}). At each target temperature, the sample was equilibrated for 3 min before spectrum acquisition to monitor the evolution of surface species during thermal regeneration.

4.4 Dynamic light scattering (DLS) measurements

The hydrodynamic diameter and size distribution of the TRCNF/PEI were determined using a Zetasizer Ultra instrument (Malvern Panalytical, UK). For analysis, an aqueous dispersion of the microgels with a final concentration of 0.006 wt% was prepared. Prior to dilution and measurement, the sample was homogenized in deionized water by magnetic stirring for 10 min. Measurements were performed at 25 °C after a 300 s equilibration period. The multi-angle dynamic light scattering mode was utilized, incorporating data from three detection angles (173°, 90°, and 13°) to ensure angle-independent results. The average hydrodynamic diameter was derived from the autocorrelation function using the cumulants analysis method.

Author Contributions

J. Ren synthesized materials, designed and conducted the experiments, analyzed data, and drafted the manuscript. P. Liu implemented spectroscopies. Y. Qin and X. Yuan assisted with the thermogravimetric analysis (TGA). X. Cao and T. Zhou helped with the dynamic breakthrough experiments. J. Zeng conceived the idea, supervised the project, and provided funding.

Acknowledgements

This work is supported by the National Natural Science Foundation of China (No. 52505525), the HKUST (Guangzhou) startup grant, the Guangzhou Municipal Science and Technology Bureau (No. 2025A03J3951 and No. 2025A04J4329), and the Guangdong Provincial Project (2023QN10L094). We acknowledge the supports from Brilliant Energy Science and Technology Lab (BEST Lab) at the Hong Kong University of Science and Technology (Guangzhou).

Conflict of Interest

The authors declare no conflict of interest.

References

1 J. Meckling and E. Biber, *Nat. Commun.,* 2021, **12**, 2051.

2 E. S. Sanz-Perez, C. R. Murdock, S. A. Didas and C. W. Jones, *Chem. Rev.,* 2016, **116**, 11840–11876.

3 S. M. Smith, Geden, O., Nemet, G., Gidden, M., Lamb, W. F., Powis, C., Bellamy, R., Callaghan, M., Cowie, A., Cox, E., Fuss, S., Gasser, T., Grassi, G., Greene, J., Lück, S., Mohan, A., Müller-Hansen, F., Peters, G., Pratama, Y., Repke, T., Riahi, K., Schenuit, F., Steinhauser, J., Strefler, J., Valenzuela, J. M., and Minx, J. C., *The State of Carbon Dioxide Removal – 1st Edition,* The University of Manchester Research, 2023.

4 R. Socolow, Desmond, M., Aines, R., Blackstock, J., Bolland, O., Kaarsberg, T., Lewis, N., Mazzotti, M., Pfeffer, A., Sawyer, K., Siirola, J., Smit, B., and Wilcox, J., *Direct Air Capture of* CO_2 *with Chemicals: A Technology Assessment for the APS Panel on Public Affairs,* 2011.

5 International Energy Agency, *Direct Air Capture A key technology for net zero*, 2022.

6 J. Artz, T. E. Muller, K. Thenert, J. Kleinekorte, R. Meys, A. Sternberg, A. Bardow and W. Leitner, *Chem. Rev.,* 2018, **118**, 434–504.

7 H. Azarabadi and K. S. Lackner, *Appl. Energy,* 2019, **250**, 959–975.

8 M. N. Dods, S. C. Weston and J. R. Long, *Adv. Mater.,* 2022, **34**, e2204277.

9 J. A. Wurzbacher, C. Gebald, S. Brunner and A. Steinfeld, *Chem. Eng. J.,* 2016, **283**, 1329–1338.

10 D. W. Keith, G. Holmes, D. St. Angelo and K. Heidel, *Joule,* 2018, **2**, 1573–1594.

11 T. H. Kwan and Q. Yao, *Int. Commun. Heat Mass Transfer,* 2022, **139**, 106459.

12 K. Z. House, A. C. Baclig, M. Ranjan, E. A. van Nierop, J. Wilcox and H. J. Herzog, *Proc Natl Acad Sci USA,* 2011, **108**, 20428–20433.

13 H. Bouaboula, J. Chaouki, Y. Belmabkhout and A. Zaabout, *Chem. Eng. J.,* 2024, **484**, 149411.

14 M. Ozkan, S. P. Nayak, A. D. Ruiz and W. Jiang, *iScience,* 2022, **25**, 103990.

15 E. Wang, R. Navik, Y. Miao, Q. Gao, D. Izikowitz, L. Chen and J. Li, *Cell Rep. Phys. Sci.,* 2024, **5**, 101791.

16 U.S. Department of Energy, Strategy for the Carbon Negative Shot™, U.S. Department of Energy, Washington, D.C., 2025, https://www.energy.gov/fecm/strategy-carbon-negative-shot.

17 International Energy Agency, *World Energy Outlook 2024*, 2024.

18 F. Micali, M. Milanese, G. Colangelo and A. de Risi, *Appl. Therm. Eng.,* 2025, **275**, 126889.

19 C. D. Díaz-Marín and Z. J. Berquist, *Energy Environ. Sci.,* 2025, **18**, 8403–8413.

20 J. Dietsch, *FEED Study for Climeworks Direct Air Capture at a California Geothermal Facility with Long-Term Storage*, Illinois Sustainable Technology Center, 2022.

21 T. S. Nguyen and C. T. Yavuz, *Joule,* 2022, **6**, 2452–2454.

22 Y. Hu, R. Gani, K. Sundmacher and T. Zhou, *Chem. Eng. Sci.,* 2024, **298**, 120423.

23 Y. Hu, X. Li and T. Zhou, *Curr. Opin. Chem. Eng.,* 2025, **50**, 101197.

24 Lifecycle carbon intensity of electricity generation, Data source: Ember (2026) –a OurWorldinData.org/energy. https://ourworldindata.org/grapher/carbon-intensity-electricity.

View Article Online
DOI: 10.1039/D6EE01563H

25 B. Y. Li, T. Y. Lin, Y. J. Lai, T. H. Chiu and Y. C. Yeh, *Small,* 2025, **21**, e2407420.

26 Z. Li, N. J. Van Zee, F. S. Bates and T. P. Lodge, *ACS Nano,* 2019, **13**, 1232–1243.

27 J. Chen, Z. Wang, S. Li, Q. Xie, C. Ma and G. Zhang, *Adv. Funct. Mater.,* 2025, e25696, DOI: 10.1002/adfm.202525696.

28 E. Loccufier, M. G. Abebe, J. Geltmeyer, T. Meirman, O. I. K. Altan, J. F. R. Van Guyse, E. Khousakoun, H. Gidik, E. Mohsenzadeh, D. Lahem, R. Hoogenboom, B. Maes and K. De Clerck, *Adv. Mater.,* 2025, e17161, DOI: 10.1002/adma.202517161.

29 W. Liu, Z. Wang, J. A. Serna, R. Debastiani, J. E. U. Gomez, L. Lu, W. Yang, Z. Dong and P. A. Levkin, *Adv. Funct. Mater.,* 2024, **34**, 2403794.

30 Y. Ji, X. Lin, H. Zhang, Y. Wu, J. Li and Q. He, *Angew Chem Int Ed Engl,* 2019, **58,** 4184–4188.

31 D. Ji, J. Liu, J. Zhao, M. Li, Y. Rho, H. Shin, T. H. Han and J. Bae, *Nat. Commun.,* 2024, **15,** 3925.

32 Y. Shi, C. Ma, L. Peng and G. Yu, *Adv. Funct. Mater.,* 2015, **25**, 1219–1225.

33 Z. Ming, J. Zhang, W. Li, S. Wang, Y. Zhang, Z. Lu, T. Zhang, Z. Zhou, Y. Xia, Y. Zhang, X. Zhou amd J. Xiong, *Adv. Mater.,* 2025, **37**, e2501809.

34 B. Arsuffi, G. Siqueira, G. Nyström, S. Titotto, T. Magrini and C. Daraio, *Adv. Funct. Mater.,* 2024, **34**, 2409864.

35 T. Buchecker, P. Schmid, I. Grillo, S. Prevost, M. Drechsler, O. Diat, A. Pfitzner and P. Bauduin, *J. Am. Chem. Soc.,* 2019, **141**, 6890–6899.

36 M. Yue, Y. Hoshino, Y. Ohshiro, K. Imamura and Y. Miura, *Angew Chem Int Ed Engl,* 2014, **53,** 2654–2657.

37 Y. Hoshino, K. Imamura, M. Yue, G. Inoue and Y. Miura, *J. Am. Chem. Soc.,* 2012, **134**, 18177.

38 Y. Liu, H. Xu, L. Zhou and J. Zhang, *Green Chem.,* 2023, **25**, 3027–3033.

39 Y. Lu, Z. Li, Y. Xie, Y. Liu, J. Zhang and L. Zong, *ACS Mater. Lett.,* 2024, **6**, 976–984.

40 C. W. H. Rajawasam, O. J. Dodo, M. A. S. N. Weerasinghe, I. O. Raji, S. V. Wanasinghe, D. Konkolewicz and N. De Alwis Watuthanthrige, *Polym. Chem.*, 2024, **15**, 219.

41 P. J. Flory and J. Rehner, Jr., *J. Chem. Phys.*, 1943, **11**, 512–520.

42 Y. Liang, H. Zhu, L. Wang, H. He and S. Wang, *Carbohydr. Polym.,* 2020, **249**, 116876.

43 X. Shi, W. Lu, Y. Xue, H. Zhou, F. Xue, H. He, S. Wang and S. Wang, *Chem. Eng. J.,* 2021, **424**, 130362.

44 L. Zhan, W. Lu, Q. Xiang, Z. Chen, W. Luo, C. Xu, R. Huang, S. Wang and H. He, *J. Colloid Interface Sci.,* 2025, **687**, 261–270.

45 A. Al Mohtar and M. L. Pinto, *J. Phys. Chem. C,* 2022, **126**, 5159–5166.

46 K. Coenen, F. Gallucci, B. Mezari, E. Hensen and M. Annaland, *J. CO_2 Util.,* 2018, **24**, 228.

47 J. R. Hoffman, A. E. Baumann and C. M. Stafford, *Chem. Eng. J.,* 2025, **507**, 160347.

View Article Online
DOI: 10.1039/D6EE01563H

48 J. M. Kolle, M. Fayaz and A. Sayari, *Chem. Rev.,* 2021, **121**, 7280–7345.

49 W. Lu, R. Chen, L. Zhan, Q. Xiang, R. Huang, L. Wang, S. Wang and H. He, *Nano-Micro Lett.,* 2025, **18**, 80.

50 J.Wu, Y. Chen, Y. Xu, S. Chen, H. Lv, Z. Gan, X. Zhu, R. Wang, C. Wang and T. Ge, *Matter,* 2024, **7**, 123–139.

51 J. Chen, Z. Wang, S. Li, Q. Xie, C. Ma and G. Zhang, *Adv. Funct. Mater.,* 2026, **36,** e25696.

52 S.Wu, Z. Yang, L. Chen, L.Cao, Y. Qiu, H.Ma, Q. Guan, Y. Cai, Q. Fu and S. Yu, *ACS Nano,* 2026, **20,** 6864–6874.

53 R. Wang, H. Zhao, C. Qi, X. Yang, S. Zhang, M. Li and L. Wang, *Energy,* 2022, **260**, 125045.

54 J. Fang, R. Wang, Z. Chen, H. Zhou, L. Wang, Q. Li, S. Zhang and L. Wang, *Sep. Purif. Technol.,* 2025, **359**, 130475.

55 R. Wang, C. Qi, Z. Jian, H. Zhao, P. Zhang, S. An, Q. Li and L. Wang, *Fuel,* 2024, **359**, 130382.

56 A. Kiani, K. Jiang and P. Feron, *Front. Energy Res.,* 2020, **8**, 92.

57 Z. Zhou, T. Ma, H. Zhang, S. Chheda, H. Li, K. Wang, S. Ehrling, R. Giovine, C. Li, A. H. Alawadhi, M. M. Abduljawad, M. O. Alawad, L. Gagliardi, J. Sauer and O. M. Yaghi, *Nature,* 2024, **635**, 96–101.

View Article Online
DOI: 10.1039/D6EE01563H

Data availability

The data supporting this article have been included in the main text and the supplementary information (SI).